https://ntrs.nasa.gov/search.jsp?R=20190001883 2020-05-09T19:31:22+00:00Z

# Segregation-assisted plasticity in Ni-based Superalloys

D. Barba[a], T.M. Smith[b], J. Miao[c,d], M.J. Mills[c,d], R.C. Reed[a,e]

[a]*Department of Engineering Science, University of Oxford, Parks Road, Oxford, OX13PJ, United Kingdom*
[b]*NASA Glenn Research Center 21000 Brookpark Rd. Cleveland OH 44135 USA*
[c]*Center for Electron Microscopy and Analysis, The Ohio State University, Columbus, OH 43212, USA*
[d]*Department of Materials Science and Engineering, The Ohio State University, Columbus, OH 43210, USA*
[e]*Department of Materials, University of Oxford, Parks Road, Oxford, OX13PH, United Kingdom*

**Abstract**

Correlative high resolution transmission electron microscopy and energy-dispersive X-ray spectroscopy are used to study deformation-induced planar faults in the single crystal superalloy MD2 crept at 800 °C and 650 MPa. Segregation of Cr and Co at microtwins, APBs, CISFs/SISFs and CESFs/SESFs is confirmed and quantified. The extent of this is found to depend upon the fault type, being most pronounced for the APB. The CESF/SESF is studied in detail due to its role as a precursor of the microtwins causing the majority of plasticity under these conditions. Quantitative modelling is carried out to rationalize the findings; the experimental results are consistent with a greater predicted velocity for the lengthening of the CESF/SESF – compared with the other types of fault – and hence confirm its role in the diffusion-assisted plasticity needed for the microtwinning mechanism to be operative.

*Keywords:* Ni-based Superalloy, planar faults, segregation, diffusion, creep plasticity, phase transformation, STEM, EDX

## 1. Introduction

Planar faults such as anti-phase boundaries (APBs) and superlattice stacking faults (SSFs) of various flavors – intrinsic (SISF), extrinsic (SESF) or complex (CSF) – are of crucial importance to the deformation behavior of intermetallic compounds, and alloys which contain phases based upon them [1, 2, 3]. This is because dislocations, even when dissociated, cannot pass through the ordered

lattice without their creation in one form or another. A corollary is a range of interesting but practically important plastic phenomena: anomalous yielding, a substantial strain hardening effect and an anisotropy of tensile/compressive behavior which is non-Schmidian [4, 5, 6].

The above applies particularly to the case of the Ni-based superalloys [7, 8] – because of the presence of a significant fraction of the $\gamma'$-phase of ordered $L1_2$ crystallography. Well known is the substantial influence of the APB and its role in the temperature-dependence of the yield point which is positive rather than negative, at least until a temperature of approximately 800 °C is reached [9]; the accepted explanation is the anisotropy of the APB energy and in particular the role of cross-slip from {111} to the {001} plane [10, 11, 12]. But the factors leading to softening beyond 800 °C are not well understood [13] and further systematic experimentation is needed to understand the microscopic processes arising in this temperature range. Consequently, new nano- and micro-mechanical interpretations need to be advanced, for scientific benefit and technological effect.

This paper is concerned primarily with the chemical segregation at the planar defects introduced by creep deformation in a prototype Ni-based superalloy at 800 °C. In the alloy considered, the role of microtwinning in promoting creep deformation at such temperature has been proven [14]; nonetheless, the factors promoting nucleation and propagation of such microtwins need much further clarification. First, experimental proof of chemical segregation to the different type of planar faults formed in the superalloy is presented. Second, the driving force for the segregation is rationalized and the fault lengthening problem is modeled. Finally, the implications of this segregation-assisted plastic mechanism on the strength of the superalloys are considered in detail.

## 2. Experimental Methods

### *2.1. Creep Testing*

The single crystal prototype nickel based superalloy MD2 of composition Ni-11.2Al-9.3Co-5.3Cr-2.6W-2Ta-1.65Ti-1.33Mo-0.2Si-0.03Hf (at.%) is studied [8]. The material was solution treated at 1275 °C for 8 hours, followed by ageing for 6 hours at 1080 °C and finally at 870 °C for 16 hours. The orientation of the bulk crystal was checked using backscattered electron diffraction (EBSD) analysis prior to extracting creep samples. Creep test pieces along the $\langle 011 \rangle$ direction of gauge volume $16 \times 1.6 \times 1\,\mathrm{mm}^3$ were manufactured using electrical discharge machining (EDM). Monotonic creep tensile tests were performed at 800 °C under an applied tensile load of 650 MPa, consistent with a region where a rich variety of complex deformation mechanism appears (SISFs, SESFs, microtwins and APBs) [15, 16, 17, 18]. Testing was conducted in an Instron electro-thermal mechanical testing (ETMT) machine with digital image correlation (DIC) as non-contact strain measurement. Three repetition tests were performed in order to validate the repeatability of the results.

### *2.2. STEM-EDX Analysis*

Post-mortem examination prior to scanning transmission electron microscopy (STEM) analysis was carried out in order to identify the deformation regions after creep. The samples were prepared by grinding and polishing finished with colloidal silica. The examination plane was carefully selected for subsequent STEM foil extraction, with the foil plane normal oriented along the $\langle 011 \rangle$ axis perpendicular to the tensile direction of the specimen. The preliminary study was performed using a JEOL 6500F field emission gun scanning electron microscope (FEG-SEM) using an accelerating voltage of 10 kV and probe current of 300 pA. Backscattered electron images were acquired in order to reveal the deformed regions within the sample. An overview of the faulted deformed region studied later by STEM is shown in Fig. 1b. STEM foils were extracted from these regions normal to $\langle 011 \rangle$ orientation using an FEI Helios Nanolab Dual-beam 600 focused ion beam (FIB). This assures planar faults are viewed edge-on

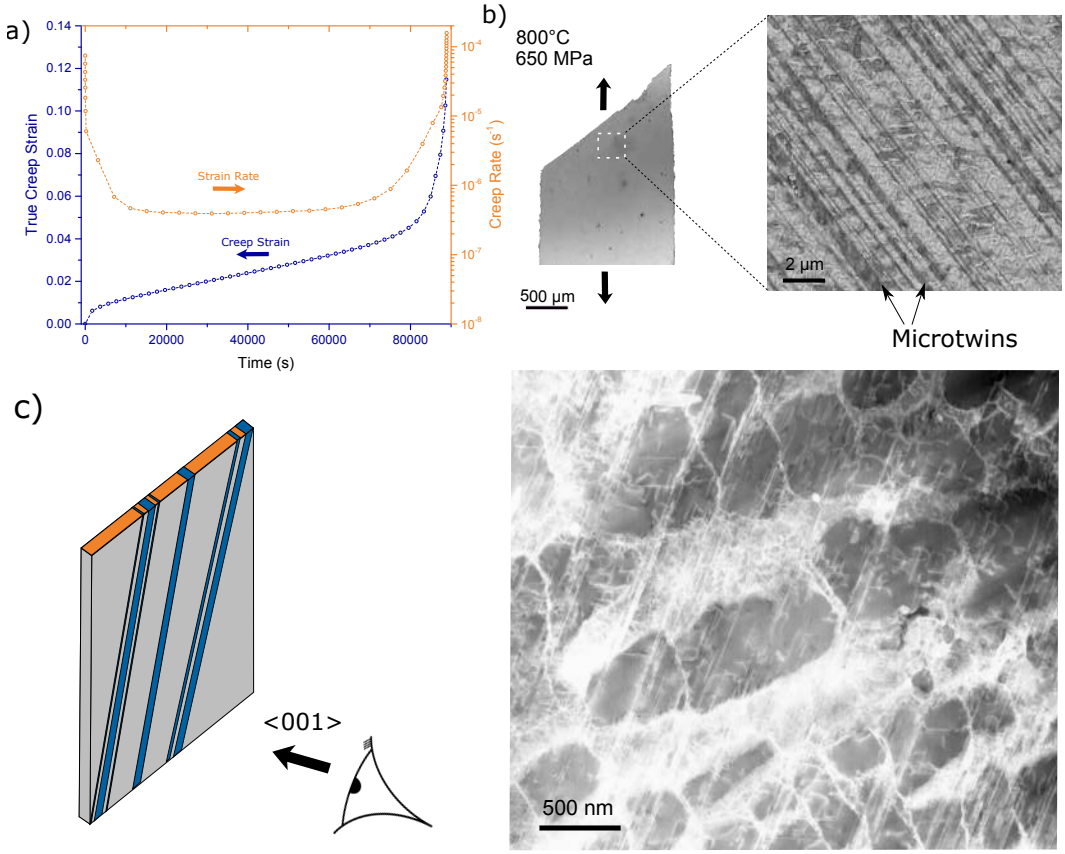


Figure 1: a) Strain and strain rate over time for ⟨011⟩ single crystal MD2 creep test at 800 °C and 650 MPa under tension; b) fracture surface of the tested specimen and SEM backscattered electron micrograph; c) detailed diagram of the STEM foil view angle relative to the crystal orientations and STEM micrograph of the deformed microstructure of the crept specimen.

using high angle annular dark field (HAADF) zone axis imaging as indicated in Fig. 1c. Samples were thinned at 5 kV and then further cleaned using a Fischione Nanomill. Energy dispersive X-ray analysis (EDX) of the foils was performed on an image-corrected Titan3$^{TM}$ 60-300 kV with a Super-X detector utilizing the Bruker Esprit software. Integrated line scans were conducted and quantified through CliffLorimer analysis [19] using experimental $K_\alpha$ energies for Ni, Co, Al, Cr and Ti. $L_\alpha$ was used for the case of Mo. The Cu specimen holder signal was avoided by using the $M_\alpha$ lines for Ta and W since the $L_\alpha$ Ta and W peaks corresponded too closely to a Cu peak to be accurately considered. Deconvolution for the W and Ta $M_\alpha$ peaks, as well as background subtraction, was used to reduce the influence of Bremsstrahlung. Higher atomic resolution STEM analysis was performed using a probe-corrected Titan3$^{TM}$ 60-300 kV.

## 3. Results

The creep strain and strain rate evolutions during the test are presented in Fig. 1a. The secondary creep stage extends for most of the test after a short period of primary creep. This is consistent with creep testing in these range of conditions along the $\langle 011 \rangle$ direction [20, 21, 22]. The fractured specimen after testing is shown in Fig. 1b. Microtwin bands following the fracture plane can be observed along an extensive region of the sample. The STEM analysis of the deformed region is presented in Fig. 1c. The image shows a high density of continuous faults preferentially along one slip direction. The existence of these faults is a consistent proof of the high activity of partial dislocations shearing at these testing conditions (800 °C-650 MPa). This high density of faults contrasts with the relatively cleaner microstructures reported by Smith et al. [2], presumably explained by the higher level of strain imposed here to the samples studied. The complex dislocation structures extend also to the $\gamma$-channels where dislocation pile-ups can be observed. Further HR-STEM confirmed the presence of SESFs, SISFs, APBs and microtwins within the planar faults, with the latter being the most repeated and accounting for most part of the plastic

deformation.

Several of these faulted structures were analyzed in detail using atomic resolution STEM. Once the type of fault was identified, chemical analysis of the fault was performed by means of EDX to study the different segregation mechanisms among them. To avoid any doubt, the segregation and diffusion processes detailed here are always referred to the shearing process within the $\gamma'$-precipitates. No segregation is observed at the $\gamma$-channels in accordance with previous findings for segregated microtwins [18, 23]. The different structures analysed are presented next.

### *3.1. Microtwins*

Two different microtwins within $\gamma'$ precipitates have been analyzed. HAADF-STEM images in the $\langle 011 \rangle$ zone axis of both microtwins are presented in Fig. 2-left. The first microtwin is in an early stage of growth, with around 15 $\{111\}$ planes thickness, while the second one is in a mature state extending over the whole field of view. The concentration profiles across the microtwins interfaces are shown in Fig. 2-right from vertically integrated EDX line scans. They confirm the segregation of Cr – a well known $\gamma$-stabilizer – at the twin interfaces. For the case of the thin twin, the interfaces were also found to be slightly enriched with respect of Mo, although the background noise from the measurements make this less clear.

Nevertheless, the cores of both twins recover the nominal concentration of the $\gamma'$-precipitate confining the segregation to just the twin interfaces. Barba et al. [14] and Smith et al. [2] have proposed a model to rationalize this phenomena. In their models there is a local shift of chemistry from $\gamma' \rightarrow \gamma$ at the microtwin interfaces. This is needed to lower the energy of the high-energy faults formed at the twin boundaries as a result of the Shockley partial shearing whereas the core of the twin recovers the perfect lattice structure.

### *3.2. Intrinsic and extrinsic stacking faults: CISF/SISF and CESF/SESF*

A HAADF-STEM image of a region containing five different planar faults is shown in Fig. 3a. These correspond to two CESFs/SESFs on a first $\{111\}$

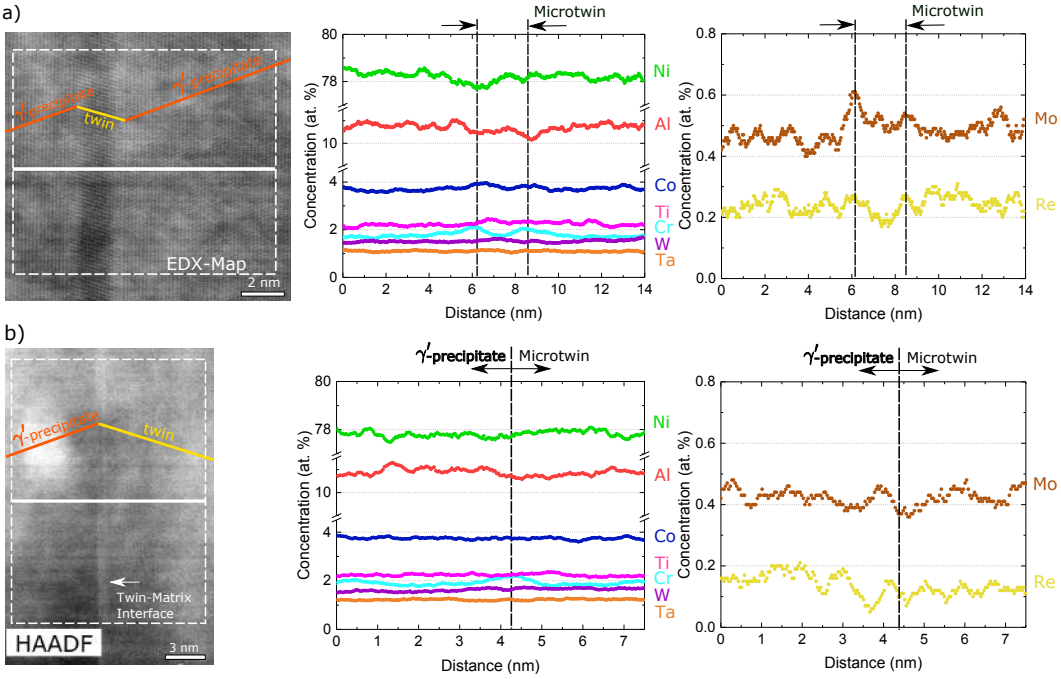


Figure 2: a) Left: HAADF-STEM detail of a microtwin showing the change of lattice orientation between the parent and twinned phase. Right: horizontal integrated EDX line scan across the twin indicated in the HAADF-STEM image; b) Left: HAADF-STEM micrograph of a $\gamma'$-twin interface showing the microtwin interface as a higher intensity line. Right: horizontal integrated EDX line scan across the twin interfaces. Twin-parent interfaces are indicated by dash-lines.

slip plane and two CESFs/SESFs and a CISF/SISF on a complementary {111} slip system. The faults can be either complex faults (CESF and CISF) or regular faults (SESF and SISF) as the present analysis cannot distinguish between them. The planar faults cut each other presenting interesting interactions and blocking the growth of some of them. Some of the interaction spots and fault ending points present a higher intensity in the HAADF-STEM image which might be related with a higher concentration of heavier elements. This observation is consistent with the previous work in ME3 alloy by Smith et al. [24]. The rationalization of these higher density regions associated with the fault growth is discussed in the following section.

The EDX maps of the faults region are presented in Fig. 3a. These maps highlight the segregation of Cr and Co along the planar faults. Conversely, Al an Ni maps show depletion of these elements along the stacking faults. The compositional changes for each fault have been quantified and they are shown as compositional profiles in Fig. 3b. They have been integrated parallel to the plane of each fault as indicated in Fig. 3a. For the case of the CISF/SISF, strong segregation of Cr and Mo is observed, while Co is segregated to a lesser extent. In contrast, an intense depletion of Ni and Al from the fault lines is observed, similarly to the microtwins. These data confirm the qualitative results of the elemental maps presented before. The same phenomenon has been observed to occur for the case of the CESFs/SESFs, being Co segregated to a slightly higher intensity than in the CISF/SISF. Non-conclusive data were found for Mo segregation in the case of the CESFs/SESFs.

### *3.3. Anti-phase boundary*

Finally, an array of planar faults containing an APB within a $\gamma'$ precipitate has been studied. A HAADF-STEM image of the dislocation/fault array is shown in Fig. 4a. Several dislocations can be observed coinciding, after atomic resolution fault analysis, with the higher intensity locations observed in the image. These locations have been reported before to be associated with clouds

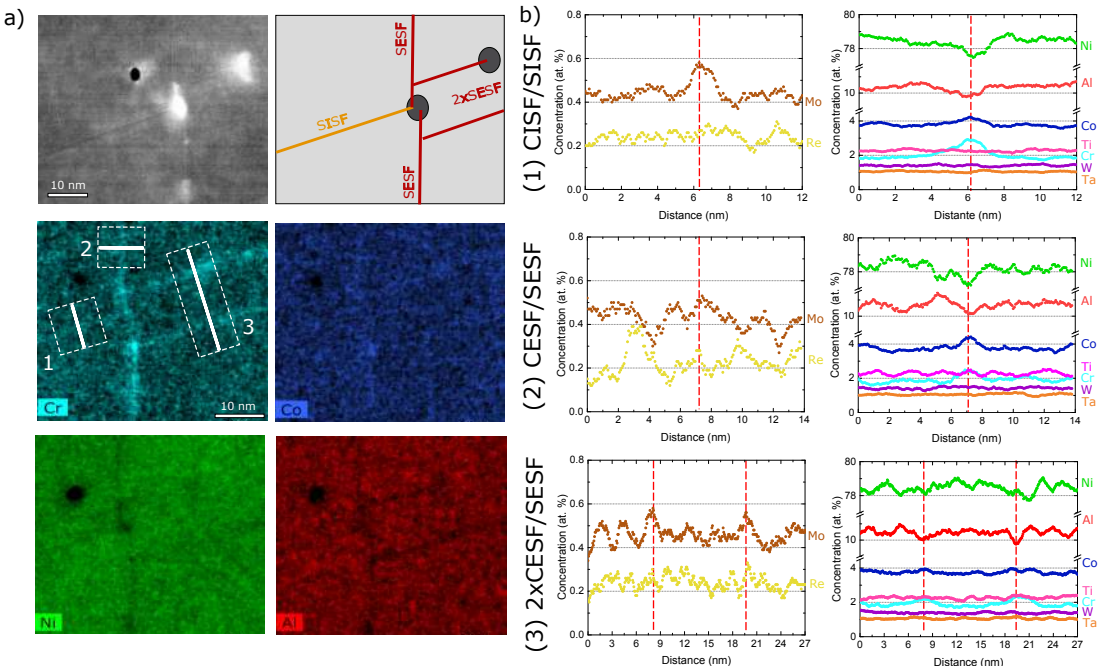


Figure 3: a) STEM micrograph of a faults structure (CISF/SISF+CESF/SESF +2xCESF/SESF) and its corresponding elemental EDX maps; b) integrated EDX line scans showing the concentration profiles across the different stacking faults detailed in (a). The positions of the faults are indicated by red lines.

of higher atomic number elements [25].

Analysis of this array of dislocations indicates that there has been interaction of the primary (horizontal) $\{111\}$ slip system with the conjugate $\{111\}$ slip system. It has been found that a series of $a/2\langle 110\rangle$ dislocations from the conjugate system are incorporated in the dislocation array of the primary slip plane. This is apparent since Burgers circuits around the individual dislocations configurations produce closure failures containing a component pointing out of the primary glide plane, see Fig. 4b. In fact, this is consistent with the presence of conjugate $a/2\langle 110\rangle$ dislocations content within the array.

The details of these interactions, and the steps leading to this configuration, are difficult to deduce from this post-deformation analysis; however, the most remarkable feature is between dislocations D1 and D2 in Fig. 4a. A higher-magnification atomic resolution STEM micrograph of the region around dislocation D2 is shown in Fig. 4b. To the left of this dislocation there is a stacking fault that could be either an SISF or CISF. To the right of dislocation D2 there is a region that apparently has perfect crystal stacking (i.e. no structural fault is present). However, closer inspection demonstrates that the higher intensity planes (corresponding to the higher atomic number, Ni-rich sublattice in the $\gamma'$ structure) are actually offset by a $a/2\langle 110\rangle$ displacement in the vicinity of the $\{111\}$ plane that would project the stacking fault located to the left of D2. Note that the contrast from this superlattice fringe intensity is not uniform, and is only clearly observed in certain regions of the image. This lack of uniformity in contrast may be due to several factors, including the presence of surface contamination in these electropolished TEM foils, as well as local compositional fluctuations that may lead to a decrease in superlattice contrast. It is noted that a similar patchiness to the superlattice contrast is found in all regions investigated, as indicated for example in Fig. 2a.

The salient point is that this region to the right of D2 appears to have the structural attributes of an APB. Compositionally, it is also distinct from the perfect $\gamma'$ regions as shown in the analysis of this region shown in the EDX maps of Fig. 4c. The elemental maps of the faults for Cr, Co and Al are presented

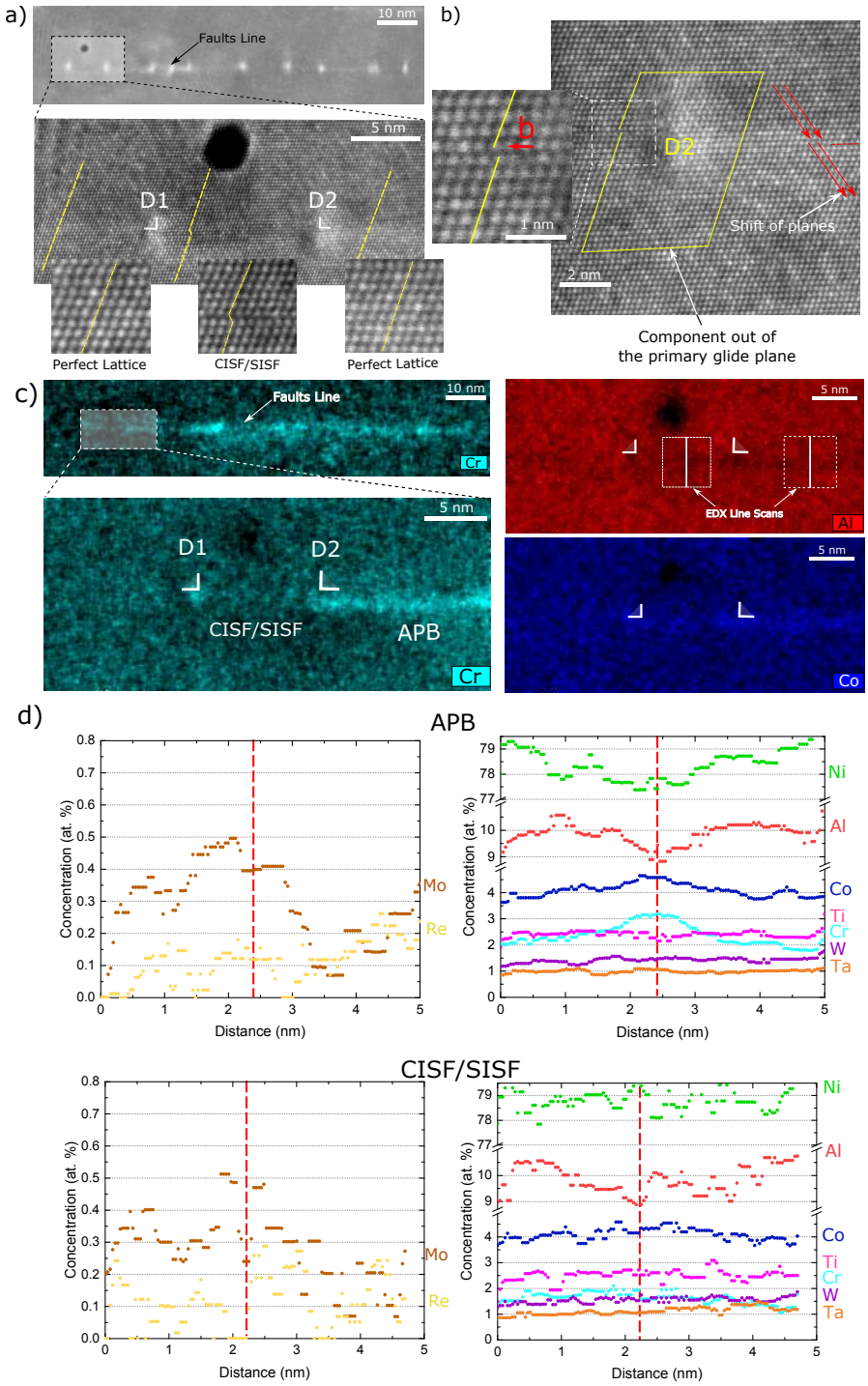


Figure 4: a) HAADF-STEM micrograph of a faults line containing multiple dislocations indicated by brighter spots (top). An atomic resolution STEM micrograph of the first two dislocations area is presented (bottom) with details of the atomic faulted structure. b) Cr, Co and Al EDX elemental map showing strong segregation along the fault line behind the second partial dislocation. This segregation suggest that the fault structure after the SISF/CISF corresponds to a energy-lowered APB.

here. The maps show that segregation of Cr is strongly localized to the APB and more limited for the case of the CISF or SISF; the same phenomenon is observed for Co. Additionally, severe depletion of Al is observed for both, the APB and the CISF or SISF. Integrated concentration profiles of the detailed region have also been computed for quantitative analysis and are presented in Fig. 4d. The quantitative results confirm the strong segregation of Co and Cr to the APB.

Summarizing, the quantitative results for the segregation of $\gamma$-stabilizers (Co, Cr and Mo) to the different types of planar faults are given in Table 1. The compositional values at the faults have been calculated from the integrated average between the mid-points of the concentration peaks. These results are averaged, if possible, from all analyzed cases for each kind of fault. The repeatability of the segregation pattern for all the different planar faults is substantial proof that the deformation kinetics of all shearing mechanisms is affected by the long-range diffusion required for extensive elemental segregation. This process is defined here as segregation-assisted shearing and it is further analyzed in the next section.

## 4. Discussion

### *4.1. Segregation-assisted shearing*

In this section, focus is put on the diffusion mechanisms controlling the lengthening of the faults. Fig. 5a shows the STEM image of the growing tip of a CESF/SESF fault. EDX elemental maps of the same region are presented in Fig. 5b. The dislocation core is surrounded by an enriched atmosphere of Cr and Co. The wake of the solute atmosphere leaves behind a segregated trail of solute. In contrast, both regions show a pronounced depletion of Al. The chemical compositions of the solute atmosphere and the $\gamma'$-precipitate are presented in Fig. 5c for comparison. They have been obtained by integration of the maps values. These results show that the local elemental composition shifts from $\gamma' \rightarrow \gamma$ equilibrium chemistry. This shift is further confirmed by the

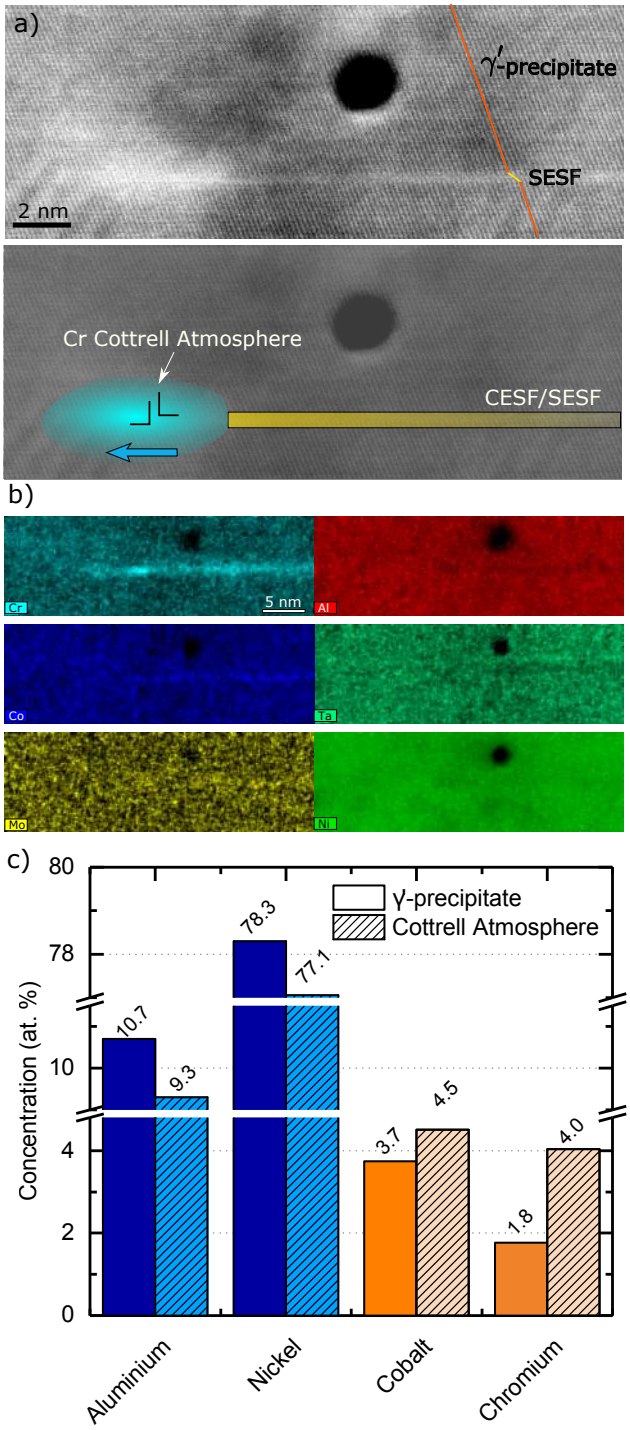


Figure 5: a) Terminating CESF/SESF with higher intensity at the growing front indicating the position of a solute-type atmosphere; b) EDX elemental maps showing segregation of Cr and Co along the fault, with a higher concentration solute atmosphere at the growing front; c) atomic composition of the solute atmosphere at the growing front of the fault and comparison with $\gamma'$ chemical composition . The composition at the fault tip is shifted locally to a $\gamma$-like structure.

extended study presented in Fig. 6 for all the type of faults presented here. These ratios are calculated as:

$$\gamma'\text{-stabilishers fraction} = \frac{(c_{\mathrm{Al}} + c_{\mathrm{Ta}} + c_{\mathrm{Ti}} + c_{\mathrm{Nb}})_{\mathrm{fault}}}{(c_{\mathrm{Al}} + c_{\mathrm{Ta}} + c_{\mathrm{Ti}} + c_{\mathrm{Nb}})_{\gamma'-\mathrm{phase}}} \quad (1)$$

$$\gamma\text{-stabilishers fraction} = \frac{(c_{\mathrm{Co}} + c_{\mathrm{Cr}} + c_{\mathrm{Mo}})_{\mathrm{fault}}}{(c_{\mathrm{Co}} + c_{\mathrm{Cr}} + c_{\mathrm{Mo}})_{\gamma'-\mathrm{phase}}} \quad (2)$$

In this figure, the ratios of $\gamma'$- and $\gamma$-stabilizers with respect to the $\gamma'$-phase values for the different faults are shown. For all the faults, a loss of $\gamma'$-stabilizers and conversely, an increase of $\gamma$-stabilizers is observed. Similar results have been reported by Smith et al. [17] for the case of SESFs on the disk-type alloy ME3. The same phenomenon is generalized in this work for CISFs/SISFs and APBs.

The results presented in Fig. 5 indicate the presence of at least two diffusion processes taking place simultaneously during dislocation shearing:

- Segregation along the fault: the Cr and Co enrichment of the different faults with respect to the surrounding $\gamma'$-precipitate composition requires long-range diffusion from the bulk. The diffusion flux is believed to be driven by the transformation of the high energy faults created by the shearing of the dislocations to low energy ones. This is achieved by stabilizing locally a $\gamma$-like structure at the fault and thus, removing the wrong-neighbors penalty. This process is illustrated schematically in Fig. 7 for the different faults observed. Obviating quantitative deviations of the different concentration levels, the segregation patterns reported show no qualitative distinction between faults. This implies that the same segregation mechanisms are likely to be present regardless of the kind fault. The specific distinctions in terms of the concentration peaks might be related to the different bonding structures and in particular, their associated fault energies as illustrated in Fig. 7.

- Solute atmosphere around the twin partials: the partial nucleus is surrounded by a Co and Cr solute cloud of a few nm in size. The solute cloud presumably moves coupled with the partial dislocations as they shear the $\gamma'$-precipitates. The enhanced enrichment of the dislocation

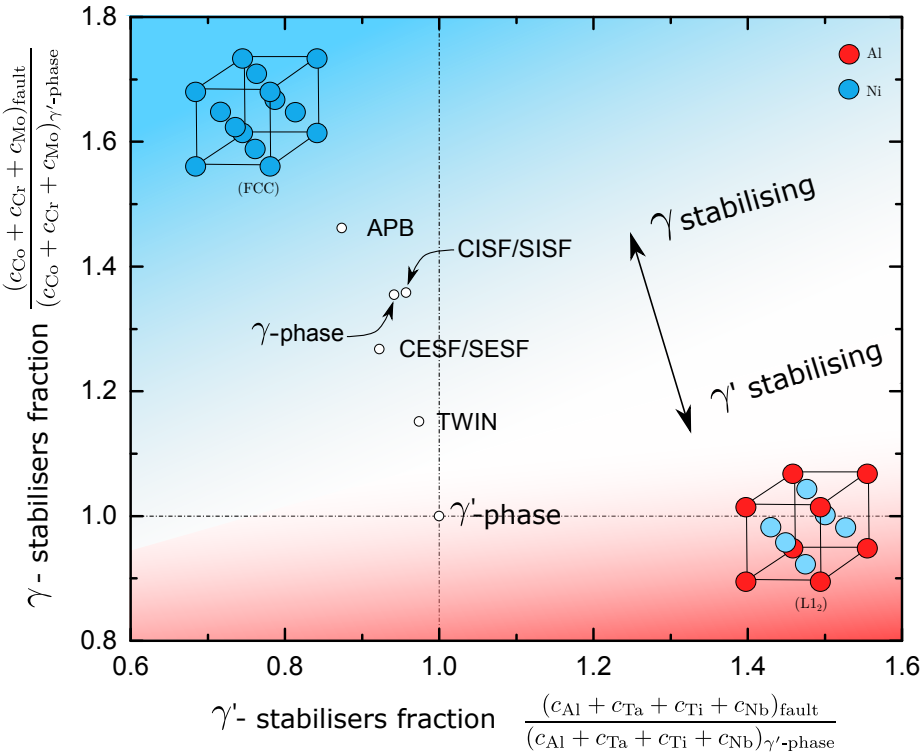


Figure 6: Ratios of $\gamma'$- and $\gamma$-stabilizers for the different faults reported in this paper. The ratios are calculated with respect to the $\gamma'$-phase values as indicated in the axes. For all the faults, a lost of $\gamma'$-stabilizers and conversely, an increase of $\gamma$-stabilizers is observed. This fact is specially intense for the case of the APB.

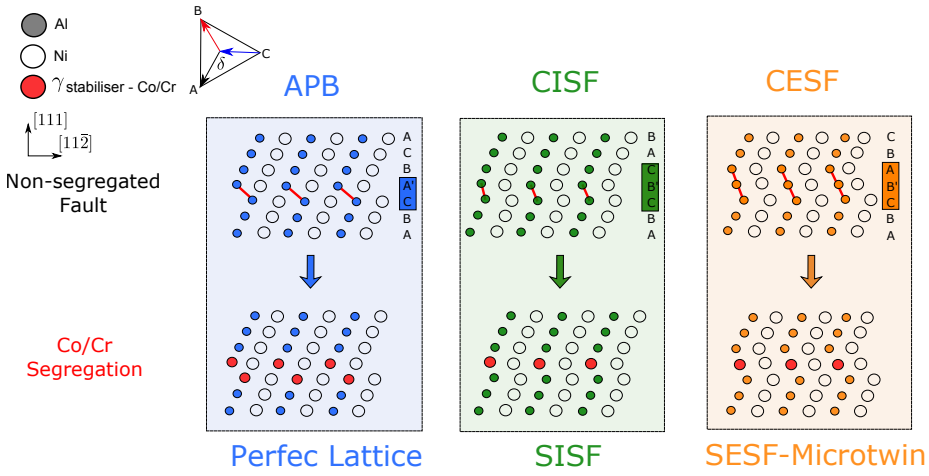


Figure 7: Atomic structures of the different faults observed in this paper (APB, SISF and SESF-Microtwin). Red lines represent high energy wrong neighbor bondings in the unsegregated faults (top) which might be suppressed or at least lowered their energy by the segregation of Ni-like atoms such as Cr and Co (bottom).

core respect to the fault might be driven by the reduction of the local strain energy associated with the dislocation. Additionally, this cloud can support, provisionally, the stabilization of the fault structure during the initial moments after the dislocation shearing and before the long-range diffusion segregation to the fault occurs.

Additionally, a third diffusion mechanism might be operative simultaneously for the case of CESFs/SESFs and microtwins. This mechanism implies the short-range atomic reshuffling of the Ni and Al lattice sites at the fault line leading to the perfect SESF-twin structure [13, 26].

Two different diffusion scales can be identified among the different diffusion mechanisms. For the latter case of the atomic reshuffling and the solute-atmosphere motion, the diffusion scale relative to the dislocation motion can be considered as short-range atomic movement. Nonetheless, the extended segregation events observed require long-range diffusion which, at the same time, implies much slower time scales. It is well known that when several mechanisms are coupled simultaneously, the slowest one is limiting the advance of the rest [27]. Therefore, in the light of this, it seems reasonable to assume that as a first approximation, the lengthening of the different faults under these conditions (800 °C and 650 MPa) is governed by the segregation of $\gamma$-stabilizers to the fault. This is further supported by the work of Smith et al. [28] where a comparative study of the lengthening rates for the different diffusion processes taking place is presented. This picture of the plastic deformation proposed here is probably applicable across a range of medium-high temperatures and high stresses. These ideas are further developed and incorporated into a mathematical model to estimate the diffusion kinetics of the different faults in the following section.

### *4.2. Estimation of fault growth rates for segregation-assisted shearing*

In this section, the model presented by Barba et al. [14] for segregation assisted growth of microtwins is extended for the case of CISFs/SISFs, CESFs/SESFs and APBs. As reported in the previous section, up to three different diffusional

processes can be acting simultaneously at the tip of the growing faults. Here, the bulk diffusion process supporting the segregation (assumed to be the time-limiting process) is modeled in order to compute the fault lengthening rates. This is done by solving the diffusion fields around the faults faithfully with the concentration data for each type of fault obtained by the EDX analysis and presented in Table 1. A schematic illustration of the lengthening problem is presented in Fig. 8a. The lengthening rate of the faults $v_\mathrm{f}$ is then computed from the mass conservation law at the growing interface:

$$v_\mathrm{f} = D_\mathrm{eff} \left.\frac{\partial c}{\partial x}\right|_\mathrm{interface} (c_\mathrm{f} - c_\mathrm{p})^{-1} \tag{3}$$

where $v_\mathrm{f}$ is the fault growth rate, $\left.\frac{\partial c}{\partial x}\right|_\mathrm{interface}$ is the concentration gradient at the growing interface, $D_\mathrm{eff} = \frac{D_\mathrm{Cr}\, c_\mathrm{Cr} + D_\mathrm{Co}\, c_\mathrm{Co}}{c_\mathrm{Cr} + c_\mathrm{Co}}$ is the effective diffusivity of Cr and Co in the $\gamma'$ parent phase and $c_\mathrm{f}$ and $c_\mathrm{p}$ are the effective Co+Cr concentrations ($c = c_\mathrm{Cr} + c_\mathrm{Co}$) at the fault and in the parent phase next to the fault tip, respectively. No conclusive results were obtained for molybdenum segregation and therefore, it is not included in this problem. It is important to notice that the APB case is slightly different from the other kind of faults as they do not extend along the whole precipitate but instead a fault of finite extension moves with the segregation line. Then the mathematical problem presented here differs slightly from the real case but in any case, the values obtained here for APBs velocities represent a lower bound. For more details of the mathematical model the reader is referred to the work of Barba et al. [14].

#### *4.2.1. Definition of model parameters*

The velocities for the different types of faults are obtained by imposing the effective segregated Cr and Co concentrations at the fault and the $\gamma'$-phase nominal concentration, both obtained from the EDX-analysis presented before. The compositions at the fault ($c_\mathrm{f}$) are the ones calculated in Table 2. The Co and Cr concentrations in the $\gamma'$ at infinity ($c_\infty$) are extracted using the averaged EDX concentrations in the $\gamma'$ far field from the twin for each fault. Additionally, the $\gamma'$ equilibrium composition ($c_\mathrm{e}$) and the chemical diffusivities of Co and Cr

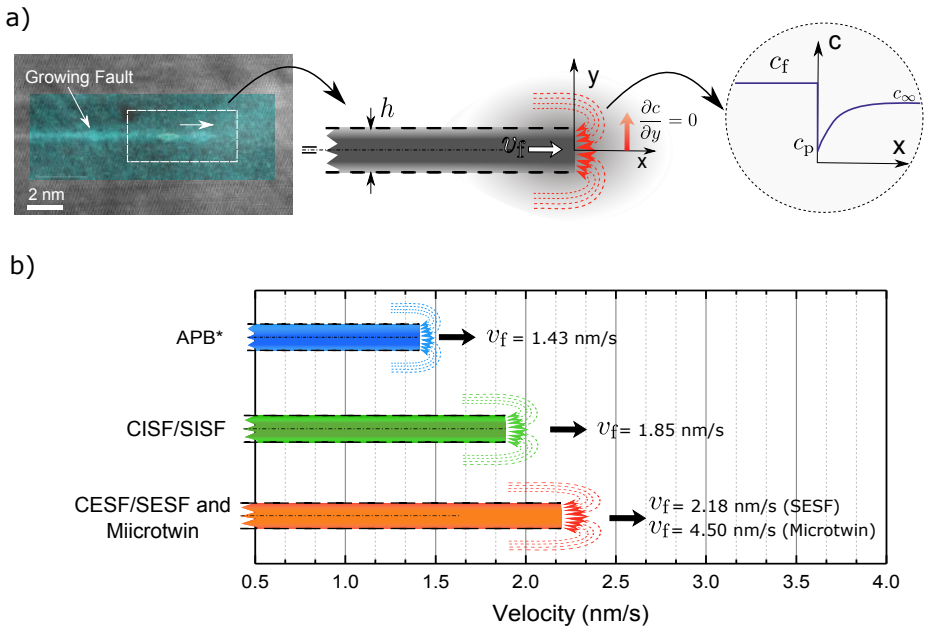


Figure 8: a) Schematics of the diffusion problem formulated for the segregation assisted growth of the different faults. A detail of the concentration profile at the fault tip is shown; b) computed fault lengthening rates for the different types of faults observed experimentally. *The growth rate value for the APB case represents an estimation of its lower limit.

($D_{\mathrm{Co}}$ and $D_{\mathrm{Cr}}$) are obtained using Thermo-Calc software (database TTNI8) and DICTRA (database MOBNI3) for equilibrium phase calculations and kinetics, respectively [29, 30]. The computed values for the relevant parameters used in the model are detailed in Table 2.

#### *4.2.2. Calculated velocities*

The lengthening rates computed for the different faults are presented in Fig. 8b. The slowest fault shearing mechanism is the APB (with the aforementioned assumptions), followed by the SISF/CISF and finally the SESF/CESF with the higher lengthening rates. It is noticeable that the fastest fault (CESF-SESF) is also the one with the highest stacking fault energy $\Gamma$, which may be unexpected ($\Gamma_{\mathrm{CESF\text{-}2}} > \Gamma_{\mathrm{CISF}} > \Gamma_{\mathrm{APB}} > \Gamma_{\mathrm{SISF}} > \Gamma_{\mathrm{SESF}}$)[31]. This may be caused by the additional combined effect of the reordering process present in the CESF/SESF lengthening [13, 26]. The reordering process can reduce the amount of segregation needed and therefore provide higher lengthening rates for CESF/SESF than the other two mechanisms. From these results it arises that shearing by Shockley partial dislocations promotes significantly the plastic flow of the alloy at high temperatures. Therefore, mechanisms that limit the plasticity to just APB shearing are desirable for strengthening the alloy as observed experimentally by Smith et al [2]. Additionally, it is noteworthy the higher level of segregation observed for APB, which may be linked with the necessity of higher amounts of $\gamma$-stabilizers in order to lower the energy of the fault.

### *4.3. Implications of the plastic-segregation events*

The segregation-assisted dislocation shearing presented here might be crucial for understanding one of the still daunting aspects of the superalloys: the sudden drop of yield-strength properties at high temperatures ($T \approx> 800\,^{\circ}\mathrm{C}$). This concept is illustrated in Fig. 9 where the diffusivities of Cr and Co are computed against the yield stress along the $\langle 001 \rangle$ orientation of the commercial superalloy CMSX-4. This superalloy has a similar composition and mechanical behavior to MD2. During plastic deformation at low temperatures

($T < 700\,^{\circ}$C), the diffusion processes are still limited and the dislocations need to enter into the $\gamma'$-precipitates without the assistance of segregation. This creates 'full-energy' faults within the $\gamma'$-precipitates which strengthen considerably the alloy. This regime is where the wide variety of standard plasticity theories for superalloys are applicable [11, 32]. As the temperature increases, the diffusion processes gradually start to become more and more important during plastic deformation. The dislocation shearing within the $\gamma'$-precipitates is now assisted by local changes in the chemistry and reordering processes and the classical strengthening mechanism for Ni-based superalloys (the high-energy faults shearing) vanishes. This provokes a reduction of the stress required to shear the $\gamma'$-precipitates and, as a consequence, a sudden drop of the plastic-strength of the alloy, as observed in Fig. 9. At really high temperatures ($T > 900\,^{\circ}$C), the dislocation climbing of $\gamma'$ precipitates and the rafting processes becomes the dominating plastic mechanisms degrading even more the mechanical strength of the alloy [33, 34, 35].

As a result, the strong effect of the local chemical changes on the creep and plastic strength must be included in future models. One of the first experimental attempts to accomplish with this purpose has been presented by Smith et al. [2], proposing the addition of certain elements (Ti, Ta and Nb) to block the effect of the $\gamma$-stabilizers and eventually strengthening the alloy. In order to push forward the temperature capabilities of these alloys, these segregation processes need to be fully integrated in multi-physics continuum models which potentially will allow to capture the dependence of the strength of the alloy on its chemical composition.

## 5. Summary and Conclusions

The single crystal superalloy MD2 deformed at 800 °C and 650 MPa has been studied. The following specific conclusions can be drawn from this study:

1. HR-STEM at atomic resolution has been used to characterize the creep deformation mechanisms occurring in this material under these conditions;

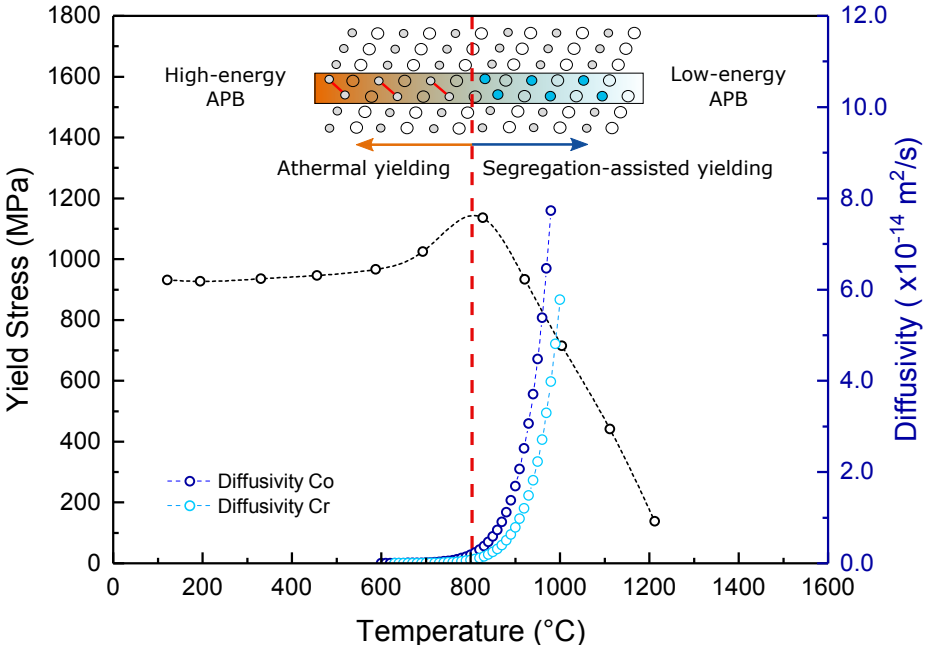


Figure 9: Correlation between the evolution of the yield stress of the single-crystal superalloy CMSX-4 [36] with temperature and the diffusivity of Cr and Co within the $\gamma'$-precipitates. The results presented in this paper suggest that at higher temperatures (T > 800 °C) the segregation to the deformation faults (APBs, CESFs/SESFs, CISFs/SISFs or microtwins) controls the strength of the alloy by changing locally its composition and therefore the fault energies necessary for dislocation glide.

these involve microtwins – in mature and embryo stages (CESFs/SESFs)– and other type of planar faults such as CISFs/SISFs or APBs.

2. All types of planar faults examined are enriched with $\gamma$-stabilizers – Cr, Co and Mo (to some extent) – with respect to the nominal $\gamma'$-phase composition of the alloy. Concomitantly, a depletion of $\gamma'$-stabilizers at the faults has been observed. This produces a shift of the chemical structure from the $\gamma'$-phase composition to the $\gamma$-phase one. This shift is especially intense for the case of APBs.
3. When the planar faults evolve to mature microtwins, the segregation is confined to the twin/matrix boundaries, so that the nominal $\gamma'$-phase composition inside the twin is recovered. This implies a contribution of diffusion within the twin to its growth.
4. The diffusion processes active during the planar fault shearing have been studied in detail. Two different diffusion scales have been identified: the long-range diffusion associated with the fault segregation process and the short-range scale of the solute cloud surrounding the dislocation core and also of the atomic-reordering.
5. The experimental observations have been introduced in an extended mathematical model so that the lengthening rates for the different faults can be calculated. The results suggest that the SISFs and SESFs are likely to promote high temperature plastic flow more effectively than the APBs.
6. These observations suggest that high temperature time-dependent plasticity is assisted by chemical changes confined locally at the faults, thus contributing to a drop in the observed strength of the alloy. This phenomenon – which changes the stress necessary for plastic deformation – needs to be accounted for in future theories for the high temperature time-dependent plasticity of these materials ($T > 700\,^{\circ}C$).

## Acknowledgments

The authors are grateful to J. Moverare and M. Segersäll for the provision of the studied material. The authors also thank S. Pedrazzini and E. Alabort for their assistance and advice. Funding from the EPSRC is acknowledged under grants EP/M50659X/1, EP/K032518/1 and and EP/K032518/1.

## References


[1] R. J. McCabe, I. J. Beyerlein, J. S. Carpenter, and N. A. Mara. *Nat. communications*, 2014.

[2] T. M. Smith, B. D. Esser, N. Antolin, A. Carlsson, R. E. A. Williams, A. Wessman, T. Hanlon, H. L. Fraser, W. Windl, D. W. McComb, and M. J. Mills. *Nat. Commun.*, 2016.

[3] H. Van Swygenhoven, P. M. Derlet, and A. G. Froseth. *Nat Mater*, 2004.

[4] Q. Qin and J. L. Bassani. *J. Mech. Phys. Solids*, 1992.

[5] N. Tsuno, S. Shimabayashi, K. Kakehi, C. M. F. Rae, and R. C. Reed. *Superalloys 2008*, 2008.

[6] Q. Qin and J. L. Bassani. *J. Mech. Phys. Solids*, 1992.

[7] S. Keshavarz, A. C. E. Ghosh, S.and Reid, and S. A. Langer. *Acta Mater.*, 2016.

[8] D. Leidermark, J. J. Moverare, S. Johansson, K. Simonsson, and S. Sjöström. *Acta Mater.*, 2010.

[9] R. C. Reed. *The superalloys: Fundamentals and applications.* 2006.

[10] I. Alvarez, A. C. Picasso, and A. J. Marzocca. *Mater. Sci. & Eng. A*, 1997.

[11] D. J. Crudden, A. Mottura, N. Warnken, B. Raeisinia, and R. C. Reed. *Acta Mater.*, 2014.

[12] A. Vattré, B. Devincre, and A. Roos. *Acta Mater.*, 2010.

[13] M. Kolbe. *Prog. Mater. Sci.*, 2001.

[14] D. Barba, D. Pedrazzini, A. Collins, A. J. Wilkinson, M. P. Moody, P. A. J. Bagot, A. Jérusalem, and R. C. Reed. *Acta Mater.*, 2017.

[15] R. R. Unocic, N. Zhou, L. Kovarik, C. Shen, Y. Wang, and M. J. Mills. *Acta Mater.*, 2011.

[16] D. M. Knowles and S. Gunturi. *Mater. Sci. Eng. A*, 2002.

[17] T. M. Smith, R. R. Unocic, H. Deutchman, and M. J. Mills. *Mater. at High Temp.*, 2016.

[18] D. Barba, S. Pedrazzini, A. Vilalta-Clemente, A. J. Wilkinson, M. P. Moody, P. A. J. Bagot, A. Jérusalem, and R. C. Reed. *Scr. Mater.*, 2017.

[19] H. Hoeft and P. Schwaab. *X-Ray Spectrom.*, 1988.

[20] M. Yamashita and K. Kakehi. *Scr. Mater.*, 2006.

[21] K. Kakehi. *Scr. Mater.*, 1999.

[22] K. Kakehi. *Metall. Mater. Transactions A*, 1999.

[23] L. P. Freund, O. M. Messé, J. S. Barnard, M. Göken, S. Neumeier, and C. M. Rae. *Acta Mater.*, 2017.

[24] T. M. Smith, B. D. Esser, N. Antolin, G. B. Viswanathan, T. Hanlon, A. Wessman, D. Mourer, W. Windl, D. W. McComb, and M. J. Mills. *Acta Mater.*, 2015.

[25] T. M. Smith Jr. *Orientation and Alloying Effects on Creep Strength in Ni-Based Superalloys*. PhD thesis, 2016.

[26] L. Kovarik, R. R. Unocic, J. Li, P. Sarosi, C. Shen, Y. Wang, and M. J. Mills. *Prog. Material Sci.*, 2009.

[27] D. Caillard and J. Martin. *Thermally Activated Mechanisms in Crystal Plasticity*, volume 8 of *Pergamon Materials Series*. 2003.

[28] T. Smith, Y. Rao, Y. Wang, M. Ghazisaeidi, and M. Mills. *Acta Mater.*, 2017.

[29] J. O. Andersson, T. Helander, L. Höglund, P. Shi, and B. Sundman. *Calphad.*, 2002.

[30] Accessed January 2015.

[31] V. A. Vorontsov, R. E. Voskoboinikov, and C. M. F. Rae. *Philos. Mag.*, 2012.

[32] E. I. Galindo-Nava, L. D. Connor, and C. M. F. Rae. *Acta Mater.*, 2015.

[33] Z. Zhu, H. Basoalto, N. Warnken, and R. C. Reed. *Acta Mater.*, 2012.

[34] R. C. Reed and C. M. F. Rae. 22 - Physical Metallurgy of the Nickel-Based Superalloys. In D. E. Laughlin and K. Hono, editors, *Physical Metallurgy (Fifth Edition)*, pages 2215–2290. Elsevier, 2014.

[35] a. Ma, D. Dye, and R. C. Reed. *Acta Mater.*, 2008.

[36] A. Sengupta, S. K. Putatunda, L. Bartosiewicz, J. Hangas, P. J. Nailos, M. Peputapeck, and F. E. Alberts. *J. Mater. Eng. Perform.*, 1994.

**Figure 1** – a) Strain and strain rate over time for $\langle 011 \rangle$ single crystal MD2 creep test at 800 °C and 650 MPa under tension; b) fracture surface of the tested specimen and SEM backscattered electron micrograph; c) detailed diagram of the STEM foil view angle relative to the crystal orientations and STEM micrograph of the deformed microstructure of the crept specimen.

**Figure 2** – a) Left: HAADF-STEM detail of a microtwin showing the change of lattice orientation between the parent and twinned phase. Right: horizontal integrated EDX line scan across the twin indicated in the HAADF-STEM image; b) Left: HAADF-STEM micrograph of a $\gamma'$-twin interface showing the microtwin interface as a higher intensity line. Right: horizontal integrated EDX line scan across the twin interfaces. Twin-parent interfaces are indicated by dash-lines.

**Figure 3** – a) STEM micrograph of a faults structure (CISF/SISF+CESF/SESF +2xCESF/SESF) and its corresponding elemental EDX maps; b) integrated EDX line scans showing the concentration profiles across the different stacking faults detailed in (a). The positions of the faults are indicated by red lines.

**Figure 4** – a) HAADF-STEM micrograph of a faults line containing multiple dislocations indicated by brighter spots (top). An atomic resolution STEM micrograph of the first two dislocations area is presented (bottom) with details of the atomic faulted structure. b) Cr, Co and Al EDX elemental map showing strong segregation along the fault line behind the second partial dislocation. This segregation suggest that the fault structure after the SISF/CISF corresponds to a energy-lowered APB.

**Figure 5** – a) Terminating CESF/SESF with higher intensity at the growing front indicating the position of a solute-type atmosphere; b) EDX elemental maps showing segregation of Cr and Co along the fault, with a higher concentration solute atmosphere at the growing front; c) atomic composition of the

solute atmosphere at the growing front of the fault and comparison with $\gamma'$ chemical composition . The composition at the fault tip is shifted locally to a $\gamma$-like structure.

**Figure 6** – Ratios of $\gamma'$- and $\gamma$-stabilizers for the different faults reported in this paper. The ratios are calculated with respect to the $\gamma'$-phase values as indicated in the axes. For all the faults, a lost of $\gamma'$-stabilizers and conversely, an increase of $\gamma$-stabilizers is observed. This fact is specially intense for the case of the APB.

**Figure 7** – Atomic structures of the different faults observed in this paper (APB, SISF and SESF-Microtwin). Red lines represent high energy wrong neighbor bondings in the unsegregated faults (top) which might be suppressed or at least lowered their energy by the segregation of Ni-like atoms such as Cr and Co (bottom).

**Figure 8** – a) Schematics of the diffusion problem formulated for the segregation assisted growth of the different faults. A detail of the concentration profile at the fault tip is shown; b) computed fault lengthening rates for the different types of faults observed experimentally. *The growth rate value for the APB case represents an estimation of its lower limit.

**Figure 9** – Correlation between the evolution of the yield stress of the single-crystal superalloy CMSX-4 [36] with temperature and the diffusivity of Cr and Co within the $\gamma'$-precipitates. The results presented in this paper suggest that at higher temperatures ($T > 800\,^{\circ}C$) the segregation to the deformation faults (APBs, CESFs/SESFs, CISFs/SISFs or microtwins) controls the strength of the alloy by changing locally its composition and therefore the fault energies necessary for dislocation glide.

Table 1: Averaged values for the concentrations of Cr and Co at the faults (or fault interfaces for microtwins) and at the $\gamma'$ precipitate. The concentrations at the faults are averaged-integrated assuming the cut-off point to be half of the peak. When several faults of the same type where available (for twins and SESFs) the concentration values are standard-averaged values between the same type of faults.

| | Fault | | $\gamma'$-bulk | |
|---|---|---|---|---|
| Fault | $c_{\mathrm{Cr}}$ (at.%) | $c_{\mathrm{Co}}$(at.%) | $c_{\mathrm{Cr}}$(at.%) | $c_{\mathrm{Cr}}$ (at.%) |
| Twin | 2.10 | 3.83 | 1.79 | 3.70 |
| SESF | 2.42 | 4.10 | 1.80 | 3.66 |
| SISF | 2.87 | 4.19 | 1.84 | 3.71 |
| APB | 3.18 | 4.57 | 1.82 | 3.19 |

Table 2: Parameters used for calculating the faults dislocation velocities in MD2 Ni-based superalloy.

| $D_{\mathrm{Co}}$ ($\mathrm{m}^2/\mathrm{s}$) | $D_{\mathrm{Cr}}$ ($\mathrm{m}^2/\mathrm{s}$) | $D_{\mathrm{effe}}$ ($\mathrm{m}^2/\mathrm{s}$) | $c_{\mathrm{e}}$(%) | $h_{\mathrm{t}}$(m) |
|---|---|---|---|---|
| $2.35\times10^{-18}$ | $1.77\times10^{-18}$ | $2.10\times10^{-18}$ | 4.99 | $7/3\sqrt{3}\times10^{-10}$ |